aerospace

MDPI

Article

Numerical Investigation of Stall Characteristics of Common Research Model Configuration Based on Zonal Detached Eddy Simulation Method

Xin Zhang [1], Heng Zhang [2,*] and Jie Li [1]

[1] School of Aeronautics, Northwestern Polytechnical University, Xi'an 710072, China; higgsbosonx@163.com (X.Z.); lijieruihao@nwpu.edu.cn (J.L.)
[2] School of Aerospace Engineering, Tsinghua University, Beijing 100084, China
* Correspondence: qwedc0919@163.com

Abstract: A zonal detached eddy simulation (ZDES) method, based on the two-equation *k-ω* SST turbulence model, was employed to predict stall characteristics and capture small-scale vortex structures in the wake region of the main wing under the post-stall condition of the Common Research Model (CRM) configuration. Additionally, the unsteady Reynolds-averaged Navier–Stokes (URANS) method was utilized for performance comparison in resolving small-scale vortices with ZDES. The results revealed a pronounced lateral flow on the wing, induced by the low-pressure region of the inner wing at post-stall angles of attack. Due to the downwash effect, the horizontal tail was influenced by the vortices in the wake region of the main wing, which the URANS method did not capture adequately. As the angle of attack increased, the separation area on the main wing expanded from the middle of the wing towards the inner wing. Consequently, the vortex structures in the wake region of the main wing became more intricate, and the primary peak of the lift coefficient spectrum shifted to the low-frequency region.

Keywords: unsteady aerodynamics; aircraft stall; stall characteristics; fluctuating force

Citation: Zhang, X.; Zhang, H.; Li, J. Numerical Investigation of Stall Characteristics of Common Research Model Configuration Based on Zonal Detached Eddy Simulation Method. *Aerospace* **2023**, *10*, 817. https://doi.org/10.3390/aerospace10090817

Academic Editor: Anthony D. Gardner

Received: 16 August 2023
Revised: 13 September 2023
Accepted: 15 September 2023
Published: 18 September 2023

1. Introduction

The accurate prediction of aerodynamic characteristics for commercial aircraft at the boundary states of the flight envelope remains a formidable challenge in aerodynamics, with low-speed stall being a prime example. During low-speed flight at high angles of attack, the main wing experiences extensive flow separation, leading to an unsteady wake characterized by turbulent structures of varying scales. This unsteady wake, originating from the main wing, alters the flow conditions over the tail, inducing local angle-of-attack fluctuations. Such fluctuations can subsequently result in variations in unsteady loads and structural modes, potentially leading to issues related to structural fatigue. These phenomena not only influence the aircraft's handling characteristics but also pose severe safety risks. Therefore, the investigation of aerodynamic characteristics under stall conditions for civil aircraft is crucial, both for enhancing flight safety and for improving overall flight quality.

Under normal circumstances, traditional RANS methods have already demonstrated satisfactory computational results within the linear lift range. However, due to the extensive separated flow that occurs during stall, RANS methods exhibit several limitations. Due to the complexity of the full aircraft geometry, the numerical simulation requires a greater number of computational grids than ordinary airfoil models, making the implementation of LES or DNS methods clearly unfeasible under current conditions. Therefore, the use of RANS-LES hybrid methods for numerical computation of the full aircraft configuration has become an unavoidable choice for researchers.

Forsythe et al. [1] were the first to conduct a numerical analysis of the aerodynamic characteristics of the F-15E full aircraft configuration at high angles of attack during deep-stall conditions using the DES method, and they compared the results with those obtained by using the RANS method. The calculations showed that DES was able to capture the unsteady three-dimensional flow structures in the separated wake, and the aerodynamic coefficients predicted using DES were in better agreement with experimental results than those from RANS. Through a comparison of computational effort, the authors further pointed out that the computational cost of DES was about seven times that of steady RANS for the same computational grid. Forsythe and Woodson [2] further used an unstructured adaptive grid combined with the DES method to simulate a sudden stall problem in an F/A-18E wing configuration. The results further showed that adaptive grid technology improved the prediction accuracy of DES, indicating that the computational cost of DES for aerodynamic simulation was about 5 to 10 times that of RANS.

Morton et al. [3] were the first to combine adaptive grid refinement technology with DES computation to calculate the separated flow of the full F-18C aircraft configuration at a 30° angle of attack, and they analyzed the unsteady aerodynamic loads on the tail. The results showed that the lift coefficient and vortex breakdown position obtained using DES were qualitatively consistent with the relevant experimental data, and the adaptive grid refinement captured richer small-scale flow structures. In contrast, the RANS calculation resulted in an underdeveloped vortex breakdown. Tomac et al. [4] used a combined RANS-LES method with the B-L turbulence model and the Smagorinsky model for numerical simulation of low-speed, high-angle-of-attack flow for the configuration of an F-16XL. Due to the interference effects of vortex shedding, the hybrid method was significantly better than the RANS method in the calculation of the outer wing, also indicating the necessity of unsteady computation in the prediction of the full aircraft stall flow field.

Fu et al. [5] and Xiao et al. [6] used the weakly nonlinear two-equation k-ω SST model RANS, DES, and DDES methods to compute the wing –body configuration of the NASA TN D-712. By comparing the computational and experimental results, the authors pointed out that the DDES results were more reliable and could reveal more detailed flow information and vortex structures compared to the RANS mode. Waldmann et al. [7] and Lutz et al. [8] used the DDES method based on the TAU solver to numerically simulate the effects of an unsteady wake from the main wing on the tail during post-stall conditions for the NASA CRM wing–body–horizontal-tail configuration. Combined with unstructured hybrid grid generation technology, special refinement was applied to the main wing wake area, and the computational results were in good agreement with the experiments.

While the DES method offers many advantages over the RANS method, it also presents some inherent problems. Spalart [9,10] found that in some cases, the LES mode would invade the outer boundary layer, placing that region in a state between LES and RANS (neither purely RANS mode nor purely LES mode), known as the "Grey Area". Through the refinement of streamwise grids, Menter and Kunz [11] discovered that the separated flow at the trailing edge of the airfoil predicted using DES was advanced, while the RANS results were more accurate. The authors referred to this non-physical separation as grid-induced separation (GIS). This is due to the LES mode's invasion of the boundary layer and the grid resolution not reaching the level required to solve the velocity fluctuations within the boundary layer. The "Grey Area" leads to a weakening of vortex viscosity, resulting in modeled stress depletion (MSD). The depletion of modeled stress reduces the wall friction coefficient, leading to the phenomenon of grid-induced separation.

The "Grey Area" is not only present in DES-like methods but is also a challenge faced by all global RANS-LES hybrid methods [10,12,13]. To eliminate the detrimental effects of the "Grey Area" in the original DES method, Deck [14] proposed a zonal DES method. The idea of this method is to designate RANS and DES regions separately during computation. This way, the methods used in each region are clearly defined, avoiding the ambiguous definitions between different regions (i.e., the "Grey Area" phenomenon) and thereby completely avoiding the modeled stress depletion (MSD) and grid-induced

separation (GIS) triggered by the "Grey Area." Additionally, the zonal approach allows various different DES modes to operate within the same flow field according to different separation types, providing more flexibility in computation compared to global DES-like methods.

This paper constructs a zonal DES-like hybrid method based on the two-equation k-ω SST turbulence model, calculates the stall characteristics of a typical civil aircraft configuration, evaluates the performances of different computational methods, analyzes the wake evolution characteristics of the stall flow field, and deepens the understanding of the full aircraft stall characteristics. It provides a reference for the application of DES-like hybrid methods in the prediction of civil aircraft stall. In Section 2, the two-equation k-ω SST model and the zonal DES method are briefly introduced. In Section 3, the results of the ZDES and URANS methods in the post-stall condition are discussed. Concluding remarks are presented in Section 4.

2. Numerical Methodology

2.1. Numerical Schemes Used

2.1.1. Two-Equation k-ω SST Model

In this paper, the k-ω SST model proposed by Menter [15] was utilized as the base model to construct DES-like hybrid methods. The basic idea of this turbulence model is to merge the standard k-ε model [16] and the Wilcox k-ω model [17–20]; in the near-wall region, the transformed k-ε model is combined with the Wilcox k-ω model, the k-ε model is used at the boundary layer edge and free shear layer, and the standard k-ε model is used in the fully turbulent region far from the wall [16,21]. In the k-ω SST model, the k equation and Reynolds stress calculation method are the same as those in the Wilcox k-ω model, while the ε equation is merged with the ω equation after being transformed through the relationship $\varepsilon = k\omega$.

For the k-ω SST turbulence model, the conservative forms of the k and ω equations are as follows:

$$\frac{\partial(\rho k)}{\partial t} + \frac{\partial(\rho u_j k)}{\partial x_j} = P - \beta^* \rho \omega k + \frac{\partial}{\partial x_j}\left((\mu + \sigma_k \mu_t)\frac{\partial k}{\partial x_j}\right) \tag{1}$$

$$\begin{aligned}\frac{\partial(\rho\omega)}{\partial t} + \frac{\partial(\rho u_j \omega)}{\partial x_j} &= \frac{\gamma}{\nu_t} P - \beta \rho \omega^2 + \frac{\partial}{\partial x_j}\left((\mu + \sigma_\omega \mu_t)\frac{\partial \omega}{\partial x_j}\right) \\ &\quad + 2(1 - F_1)\frac{\rho \sigma_{\omega 2}}{\omega}\frac{\partial k}{\partial x_j}\frac{\partial \omega}{\partial x_j}\end{aligned} \tag{2}$$

Here, ρ is the density, k is the turbulent kinetic energy, $\sigma_k = 0.5$, $\nu_t = \mu_t/\rho$ is the turbulent eddy viscosity, μ is the molecular dynamic viscosity, and d is the distance from the grid point to the wall. The production term P is given by:

$$P = \tau_{ij}\frac{\partial u_i}{\partial x_j} \tag{3}$$

where the Reynolds stress is given by:

$$\tau_{ij} = \mu_t\left(2S_{ij} - \frac{2}{3}\frac{\partial u_k}{\partial x_k}\delta_{ij}\right) - \frac{2}{3}\rho k \delta_{ij} \tag{4}$$

$$S_{ij} = \frac{1}{2}\left(\frac{\partial u_i}{\partial x_j} + \frac{\partial u_j}{\partial x_i}\right) \tag{5}$$

The turbulent eddy viscosity μ_t and the vortex magnitude Ω are given by:

$$\mu_t = \frac{\rho a_1 k}{\max(a_1 \omega, \Omega F_2)} \tag{6}$$

$$\Omega = \sqrt{2W_{ij}W_{ij}} \tag{7}$$

$$W_{ij} = \frac{1}{2}\left(\frac{\partial u_i}{\partial x_j} - \frac{\partial u_j}{\partial x_i}\right) \tag{8}$$

In the transformed k-ε model near the wall and the standard k-ε model in the far field, different vortex viscosity calculation methods are used, which may lead to numerical instability. Therefore, a blending function is used to enable a smooth transition between the two models.

2.1.2. Zonal Detached Eddy Simulation Method

Deck [14] divides typical flow problems into three categories, as shown in Figure 1: (I) separation caused by geometric shape, where the location of separation is fixed; (II) separation caused by pressure gradient on curved surfaces, where the location of separation is uncertain; (III) separation influenced by the incoming boundary layer. This paper only focuses on the first two types of flow.

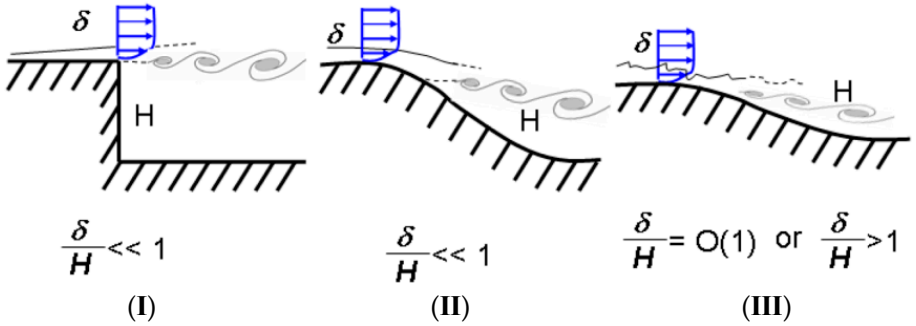

Figure 1. Classification of typical flow problems in ZDES method. (**I**): separation fixed by the geometry, (**II**): separation induced by a pressure gradient on a curved surface, (**III**): separation strongly influenced by the dynamics of the incoming boundary layer.

The ZDES method in this paper is implemented based on structured multiblock grids by defining different grid blocks to achieve the purpose of using different simulation methods in different regions within the same flow field. In a flow field composed of N grid blocks, for the nth grid block ($0 < n < N$), when $ides_n = 0$, the RANS method is used in that region; when $ides_n = 1$, the DES method is used in that region. The hybrid length scale can be written as:

$$\widetilde{l}_{\mathrm{ZDES},n} = (1 - ides_n) \times l_{\mathrm{RANS}} + ides_n \times l_{\mathrm{DES}}^{\mathrm{I\ or\ II}} \tag{9}$$

The selection of the hybrid length scale $l_{DES}^{\mathrm{I\ or\ II}}$ is specified by $imode$. When $imode_n = 1$, it corresponds to the separation of Type I flow; when $imode_n = 2$, it corresponds to the separation of Type II flow. Therefore, it can be further written as:

$$\widetilde{l}_{\mathrm{ZDES},n} = \begin{cases} l_{\mathrm{SST}}, \text{if } ides_n = 0 \\ l_{\mathrm{DES}}^{\mathrm{I}} = \min(l_{\mathrm{SST}}, C_{\mathrm{DES}}\Delta), \text{ if } ides_n = 1, imode_n = 1 \\ l_{\mathrm{DES}}^{\mathrm{II}} = l_{\mathrm{SST}} - f_d \max(0, l_{\mathrm{SST}} - C_{\mathrm{DES}}\Delta), \text{ if } ides_n = 1, imode_n = 2 \end{cases} \tag{10}$$

The subgrid scale $\Delta_{\max}$ can cause the instability of the free shear layer to be slowly delayed. Directly applying the subgrid scale $\Delta = \Delta_{\mathrm{vol}} = (\Delta x, \Delta y, \Delta z)^{1/3}$ from classical LES methods to the DES method significantly reduces the predicted level of vortex viscosity. Therefore, a new subgrid scale proposed by Chauvent [22] for the slow development of LES in the mixing layer is used in this paper. It is defined in the structured grid as follows:

$$\Delta = \Delta_\omega = \sqrt{N_x^2 \Delta y \Delta z + N_y^2 \Delta z \Delta x + N_z^2 \Delta x \Delta y} \tag{11}$$

$$\vec{N} = \frac{\left(\vec{\omega}\right)}{\|\vec{\omega}\|} \tag{12}$$

Here, $\vec{\omega}$ is the vorticity vector, and its direction is determined by the three components of the unit vector $\vec{N}$, N_x, N_y and N_z.

Thus, the definition of the subgrid scale for ZDES is as follows.

For Type I flow separation problems (where the separation location is fixed), the subgrid length scale is:

$$\Delta_{\mathrm{DES}}^{\mathrm{I}} = \Delta_{\omega} \tag{13}$$

For Type II flow separation problems (where the separation location is uncertain), the subgrid length scale is:

$$\Delta_{\mathrm{DES}}^{\mathrm{II}} = (0.5 + sign(0.5, f_d - f_{d0})) \times \Delta_{\max} + (0.5 - sign(0.5, f_d - f_{d0})) \times \Delta_{\omega} \tag{14}$$

The sign function is defined as follows:

$$\mathrm{sign}(a, b) = \begin{cases} +a \text{ , if } b \geq 0 \\ -a \text{ , if } b < 0 \end{cases} \tag{15}$$

2.2. Computational Grid and Zonal Detached Eddy Simulation Setting

The Common Research Model (CRM) configuration is a typical civil aircraft configuration designed by NASA [23], consisting of a supercritical wing and fuselage, with a design cruise Mach number of 0.85, a design lift coefficient of 0.5, a Reynolds number of 40×10^6, and a flight altitude of 12,333 m. The CRM configuration has also been used as the research model for the fourth and fifth AIAA Drag Prediction Workshops [24]. In the European ETW wind tunnel experiment [25], a 2.7% scale model was used, with a wingspan of 1.586 m, an average aerodynamic chord length of c = 0.189 m, and a reference area of S = 0.28 m^2. In addition to conventional aerodynamic force testing, the ETW experiment also included the Particle Image Velocimetry (PIV). The numerical calculations in this paper are based on the wind tunnel experimental conditions of ETW, using the CRM wing–body–horizontal-tail (0°) configuration (CRM-HTP) (the vertical tail part was fitted with a model fixing device in the experiment). Figure 2 shows the experimental model in the ETW wind tunnel.

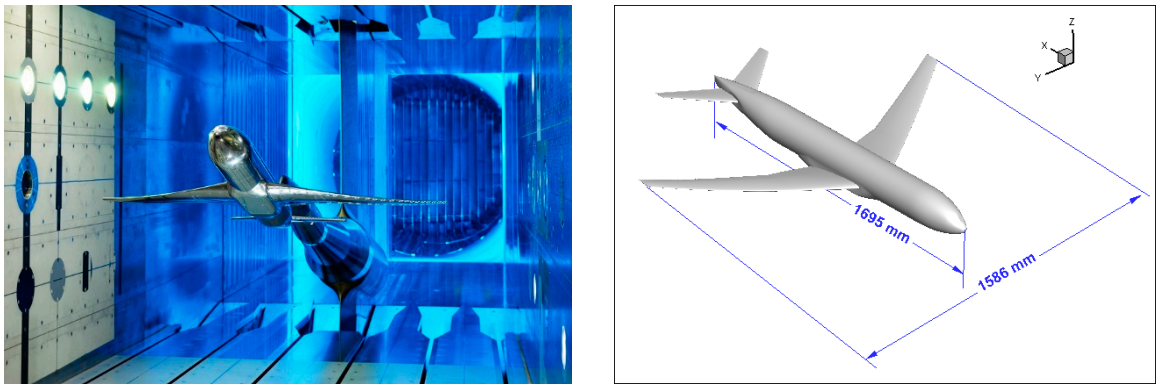

(**a**) (**b**)

Figure 2. The CRM wing–body–horizontal-tail configuration (**a**) placed in the ETW wind tunnel and (**b**) size drawing.

Figure 3 shows the division of each computational region for using the ZDES method. The RANS mode was used in the fuselage and wing undersurface regions, while the DES mode regions were in the main wing upper airfoil, tail upper airfoil, and wake regions

(areas marked with a red line in Figure 4). The grid encryption was also concentrated in these regions.

Figure 3. ZDES computation region.

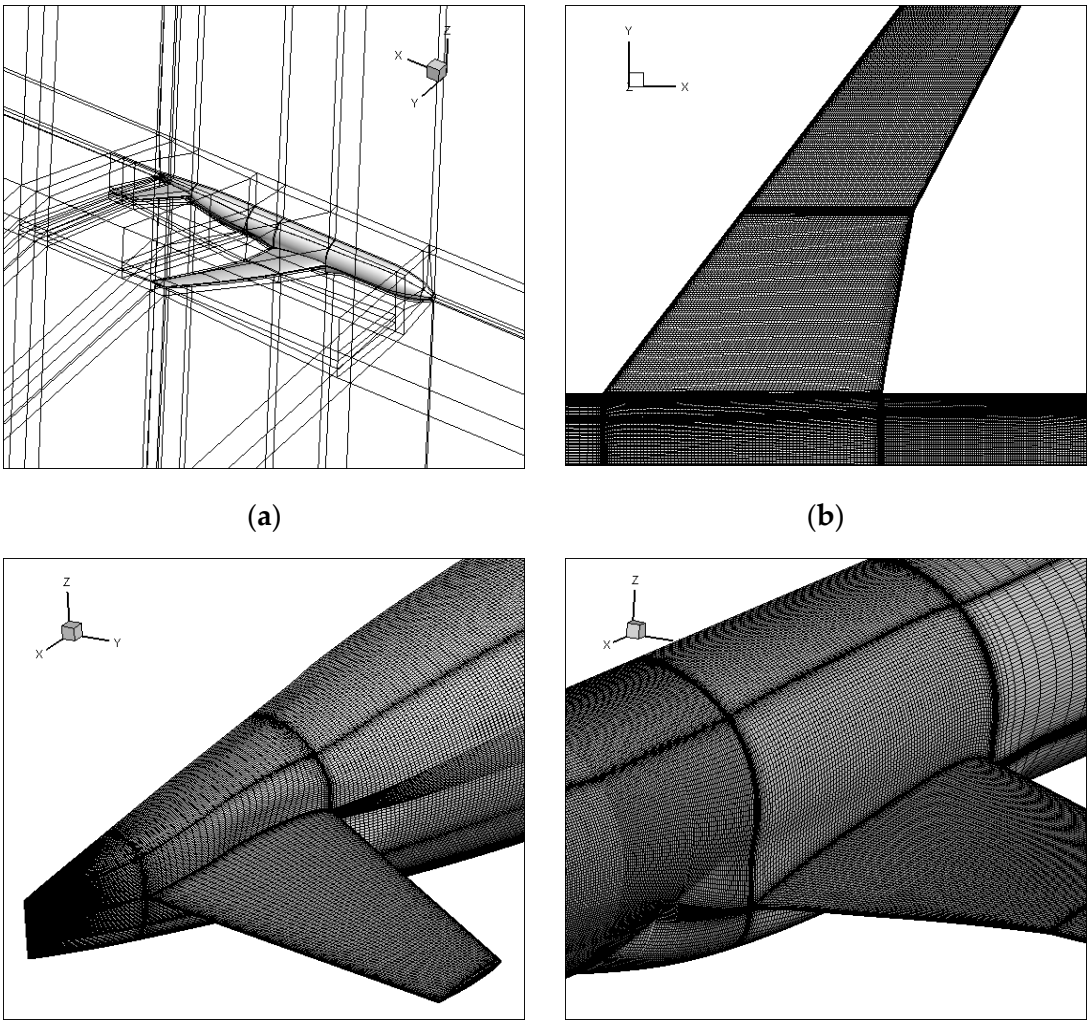

(**a**) (**b**)

(**c**) (**d**)

Figure 4. CRM computational grid (Grid A): (**a**) block topology, (**b**) the main wing, (**c**) the horizontal tail, and (**d**) the wing–body junction.

The computational conditions were selected based on experimental conditions, with an incoming flow Mach number of $Ma = 0.25$, a Reynolds number of $Re = 11.5 \times 10^6$, and a temperature of $T = 115$ K. The time step for unsteady computation was set to $\Delta t^* = 0.01$, corresponding to a physical time step of approximately $\Delta t = (\Delta t^* a_\infty)/c = 8.8 \times 10^{-6}$ s,

where $a_\infty = \sqrt{\gamma RT}$. The airflow passed through an average aerodynamic chord length in 400 time steps, and at least 25 subiterations were performed within each time step to ensure that the residual decreased by at least two orders of magnitude. All computations in the present work were carried out using an in-house compressible code with a cell-centered finite-volume formulation based on a multiblock structured grid. The unsteady computation started with the fully converged steady-state computation results as the initial field, and the statistical averaging time lasted for at least 100 chord lengths of flow-through time. The computation time for every angle of attack on the cluster machine exceeded 20,000 core hours.

2.3. Validation of the Numerical Approach

Three different multiblock structural grids were used: the fine grid had ca. 42.1 million nodes, the medium grid had ca. 14.9 million nodes, and the coarse grid had ca. 5.3 million nodes. In the region from the nose to the main wing, generally no large flow separation occurs, so the grids in this part were relatively sparse. In the space from the main wing to the tail, complex flow separation occurs under stall conditions, and the small-scale flow structures in the main wing wake affect the flow in the tail region and the overall aerodynamic calculation results; thus, the computational grids in this region were encrypted. For each grid, an O-shaped topology was used in the near-wall region to encrypt the boundary layer, and the first cell height for the body-fitted mesh was 1×10^{-6} in order to satisfy the criterion of $y+ \leq 1$. The grid resolutions of the region between the main wing and the tail wing were 3.5%*c* for the fine grid, 4.9%*c* for the coarse grid, and 7.0%*c* for the coarse grid. The block topology and local details of the fine grid are shown in Figure 3. Table 1 describes the grids in detail.

Table 1. Grid sizes.

Grid	Level	Number of Normal Nodes in Boundary Layer	Resolution of Separation Region	Total Numberof Nodes
A	Fine	51	3.5%*c*	42.1×10^6
B	Medium	35	4.9%*c*	14.9×10^6
C	Coarse	25	7.0%*c*	5.3×10^6

The angles of attack were selected as alpha = 10°, 12°, 14°, 16°, and 18° for calculations. Figure 5 shows comparisons of time-averaged lift and drag coefficients calculated with ZDES using three different grids. As can be seen, the results obtained from the three grids were in good agreement with the experiments except for the low prediction of lift coefficients at 14° and the low drag coefficients obtained from the coarse grid (Grid C) at 12°.

Figure 6 shows the pressure distributions of different stations on the main wing obtained from three different grids at 18°. The main wing spanwise stations are shown in Figure 7. It can be seen that the differences between the pressure distributions obtained from different grids were mainly reflected in the inner wing region (η = 13.1%, 20.1%, and 28.3%), compared to which the pressure distributions of the fine grid (Grid A) and the medium grid (Grid B) matched the experimental results better. In the middle and outer wing regions, the pressure distributions gradually converged, and all of them matched the experimental results well. The fine grid (Grid A) was used to analyze and discuss the stall state in all the later calculations.

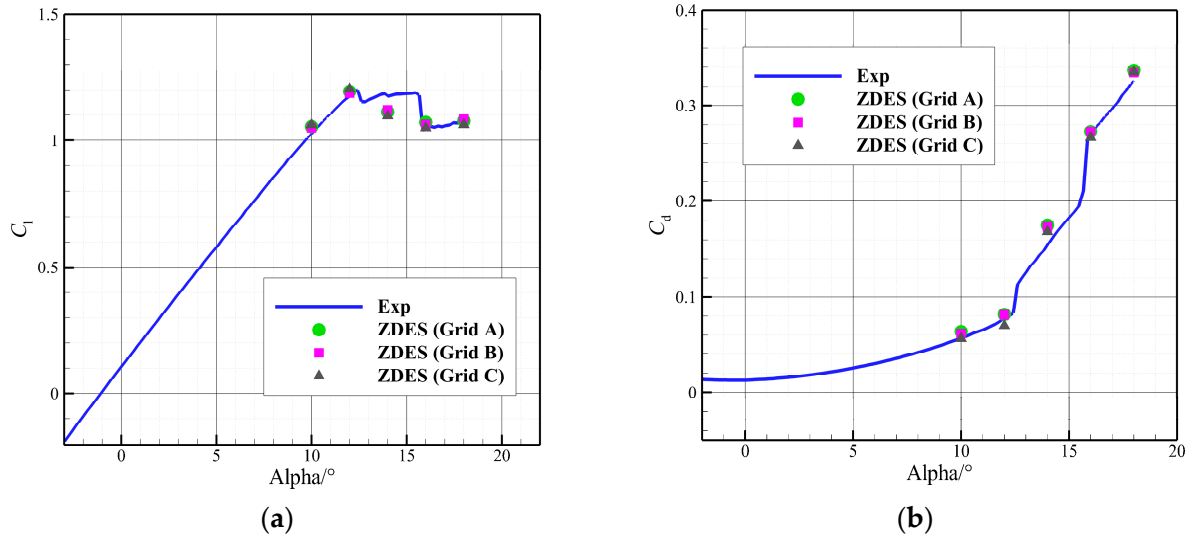

Figure 5. (**a**) Lift and (**b**) drag coefficients of different grids.

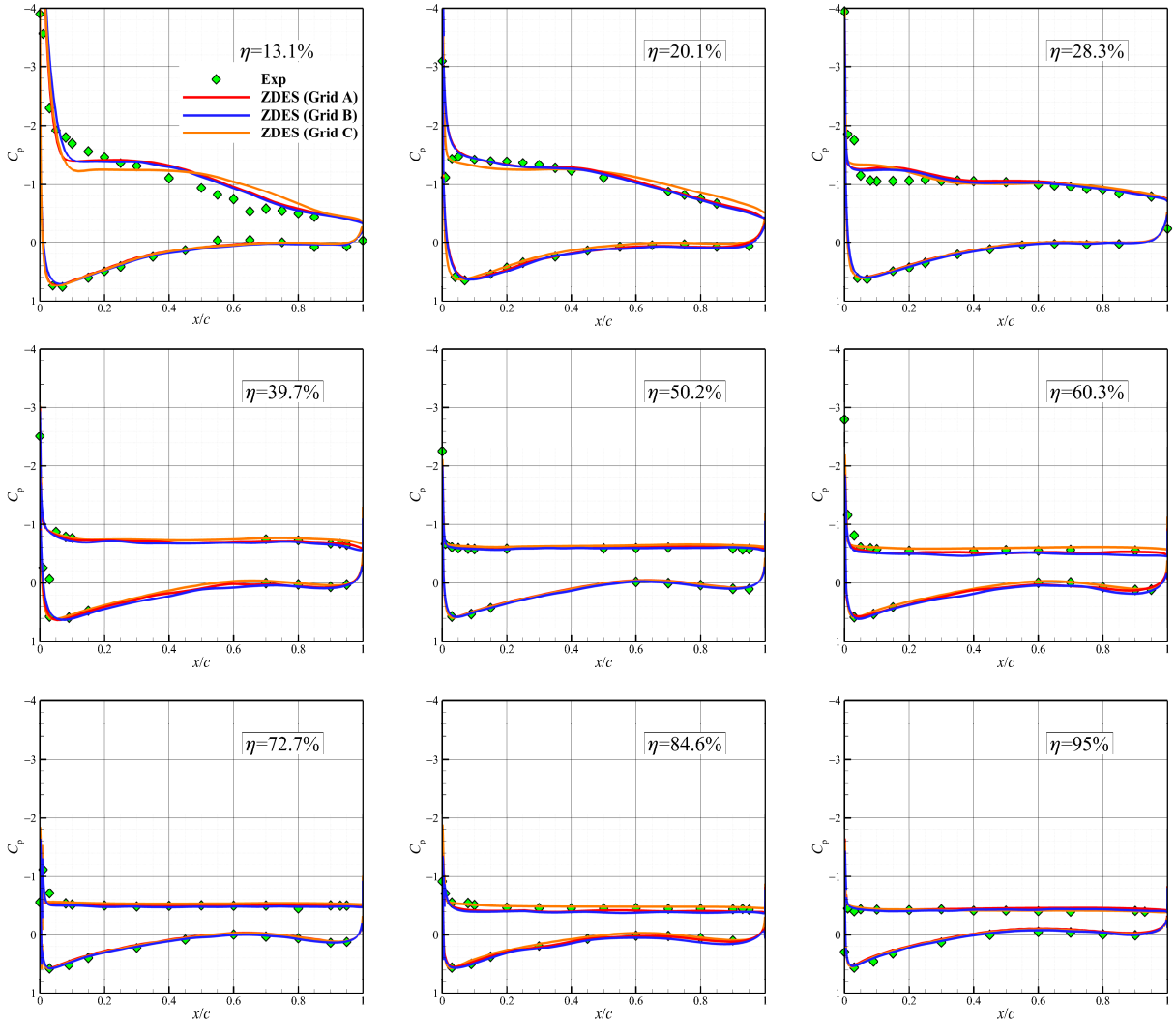

Figure 6. Pressure distributions on the main wing in different grids (alpha = 18°).

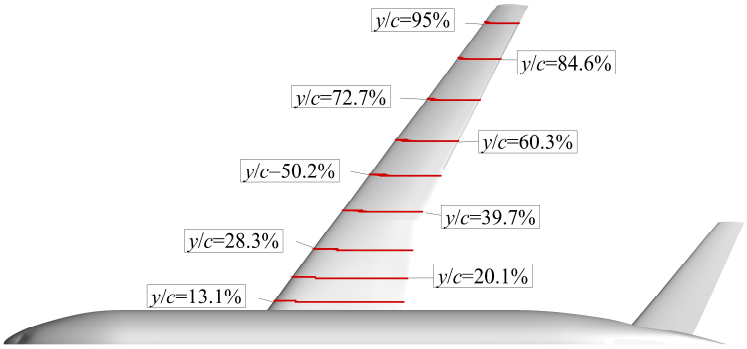

Figure 7. Schematic diagram of the main wing spanwise station.

3. Results and Discussion

The ZDES and URANS methods were used to calculate the results. The results of the two methods were compared to analyze and evaluate the aerodynamic characteristics of the CRM configuration of the whole aircraft.

Figure 8 shows the calculated mean lift coefficient and drag coefficient. At 10° and 12°, the results of the URANS and ZDES calculations were in good agreement with the experiments and consistent with the constant calculation results. At the three angles after stall, the lift and drag coefficients predicted using the ZDES method were in good agreement with the experiments, and the relative error between the lift coefficient prediction results and the experimental results was within 5.2%. With the increase in the angle, the agreement with the experiment was better in the larger angles of attack. The lift coefficients predicted using URANS, on the other hand, were significantly lower compared to the experiments, with a maximum deviation state of alpha = 14°, and the relative error reached 18%. The calculated values of the lift and drag coefficients are shown in Tables 2 and 3. And this result is very close to the results obtained by Zhao Yang et al. using the IDDES method [26]. Temporal variations in the lift and drag coefficients obtained with ZDES are shown in Figure 9, where dashed lines indicate the time-averaged results. With a rising angle of attack, the lift and drag of the whole aircraft fluctuated dramatically and increased in amplitude.

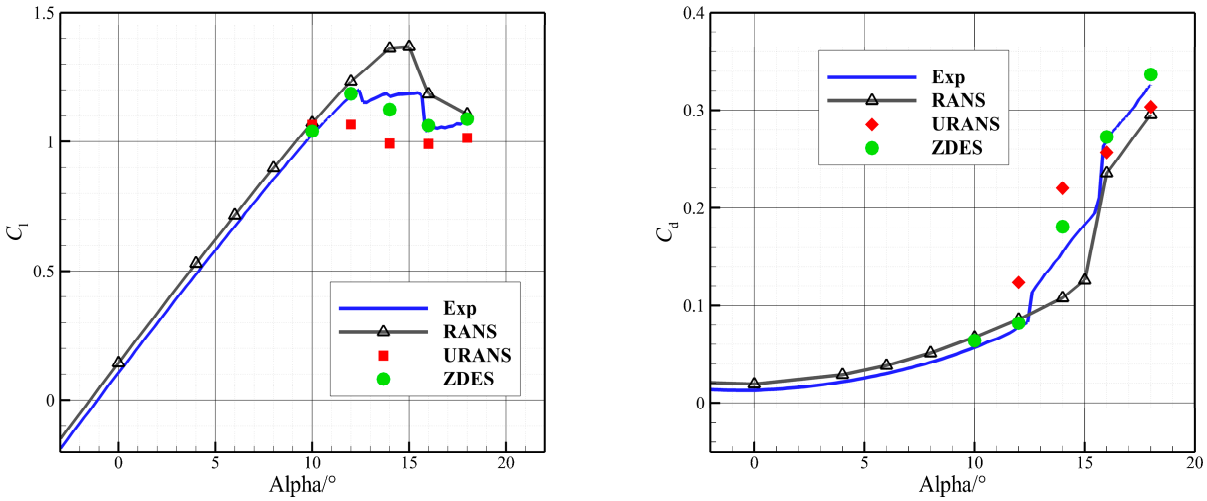

(**a**) (**b**)

Figure 8. (**a**) Lift and (**b**) drag coefficients of the whole aircraft.

Table 2. Comparison of time-averaged lift coefficients.

A	10°	12°	14°	16°	18°
Experiment	1.023	1.175	1.174	1.046	1.078
URANS	1.066	1.067	0.993	0.991	1.014
ZDES	1.054	1.194	1.113	1.071	1.077

Table 3. Comparison of time-averaged drag coefficients.

A	10°	12°	14°	16°	18°
Experiment	0.0566	0.0778	0.1556	0.2697	0.3255
URANS	0.0631	0.1237	0.2199	0.2567	0.3033
ZDES	0.0638	0.0818	0.1804	0.2727	0.3369

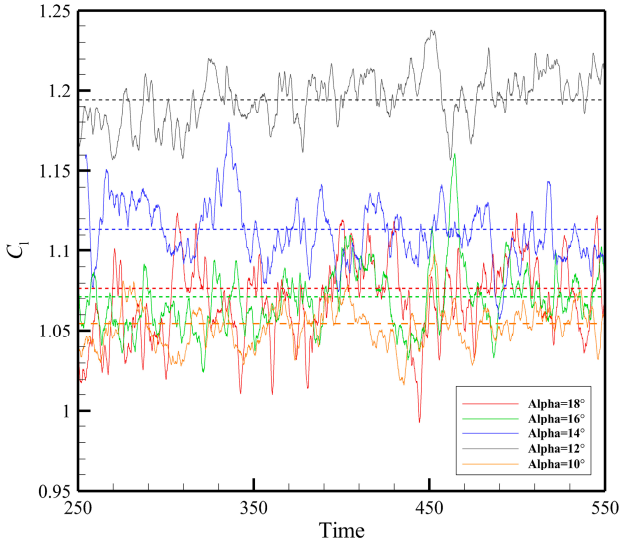

(**a**)

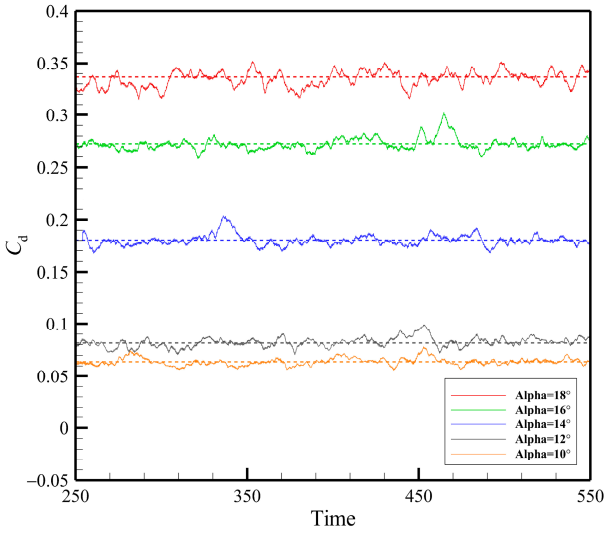

(**b**)

Figure 9. Temporal variations in (**a**) lift and (**b**) drag coefficients.

Figures 10–12 show the pressure distributions on the main wing obtained from the ZDES and URANS calculations for alpha = 14°, 16°, and 18°, respectively. The pressure distribution results obtained using URANS for the spanwise stations in the inner wing section (η = 13.1%, 20.1%, and 28.3%) were more different from the experiments, and the differences were more pronounced, especially at the larger angles of attack (16° and 18°). From the pressure distributions, the separation position obtained using URANS had a tendency to advance compared with the experiment. And the pressure distribution predicted using ZDES in the three angles was not much different from the experiment, and the separation position predicted using ZDES was in better agreement with the experiment compared with the URANS method.

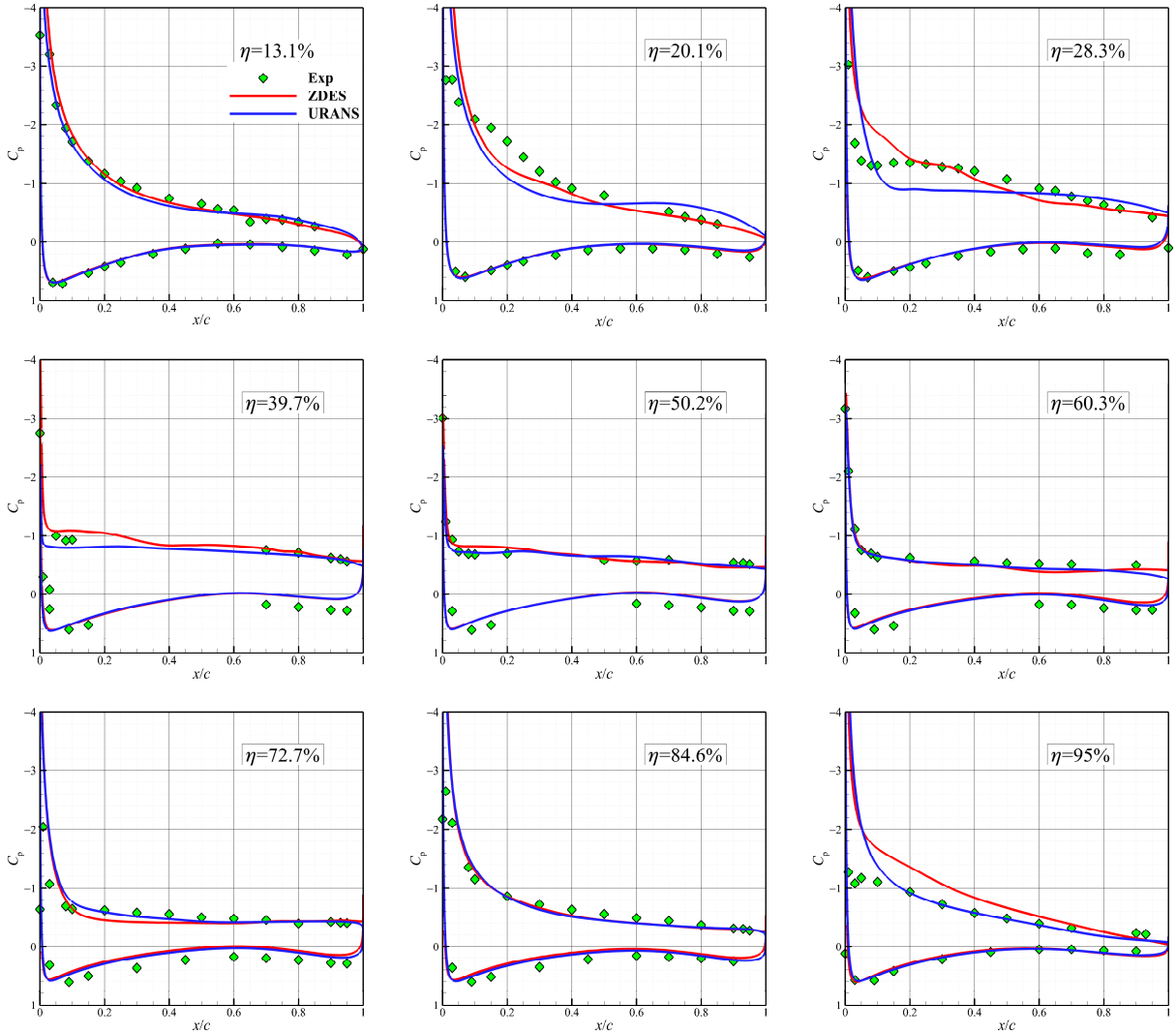

Figure 10. Pressure distribution at each station in the main wing (alpha = 14°).

At each of the spanwise stations in the middle of the main wing (η = 39.7%, 50.2%, and 60.3%), the differences between the pressure distributions obtained using URANS and the experiments were reduced compared to those in the inner wing segments, but the differences were still significant at the larger angles of attack (alpha = 18°). At the η = 39.7% position, the separation position predicted using URANS was slightly advanced compared to the experimental results. However, the ZDES calculations were still in good agreement with the experiments.

At the spanwise stations of the outer wing (η = 72.7%, 84.6%, and 95%), the pressure distributions of URANS at 14° and 16° did not differ much from the ZDES results, and

the pressure distributions obtained using the two methods were in good agreement with the experiments. At alpha = 18°, the experimental results showed that the separation had already started at the leading edge, and the pressure distribution of the wing surface obtained using ZDES was in good agreement with the experiment. While the wing surface pressures predicted using URANS were all larger than the experiments, especially at the outermost station (η = 95%), the difference in pressure was already very obvious. Comparing the calculated results of the pressure distributions, the differences between URANS and ZDES were mainly in the mid-inner section of the main wing. The pressure distributions of ZDES were in good agreement with the experiments, while the URANS results were more different from the experiments, and their predicted separation positions were advanced compared with the experimental results. At alpha = 14° and 16°, the pressure distributions obtained using the two methods were in general agreement with the experimental results. The performance of URANS in the center and outer wing also deteriorated significantly at a larger angle of attack (alpha = 18°).

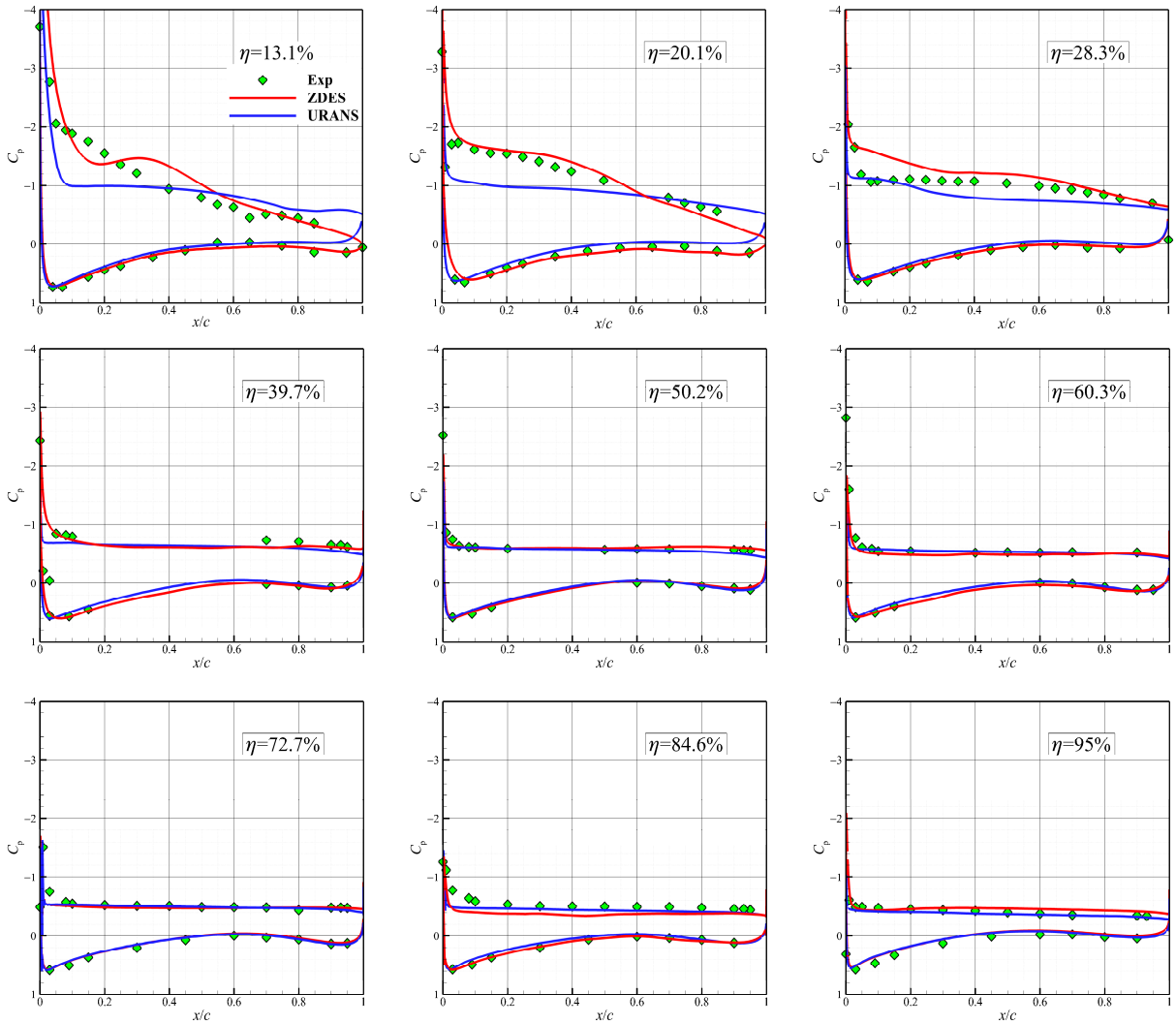

Figure 11. Pressure distribution at each station in the main wing (alpha = 16°).

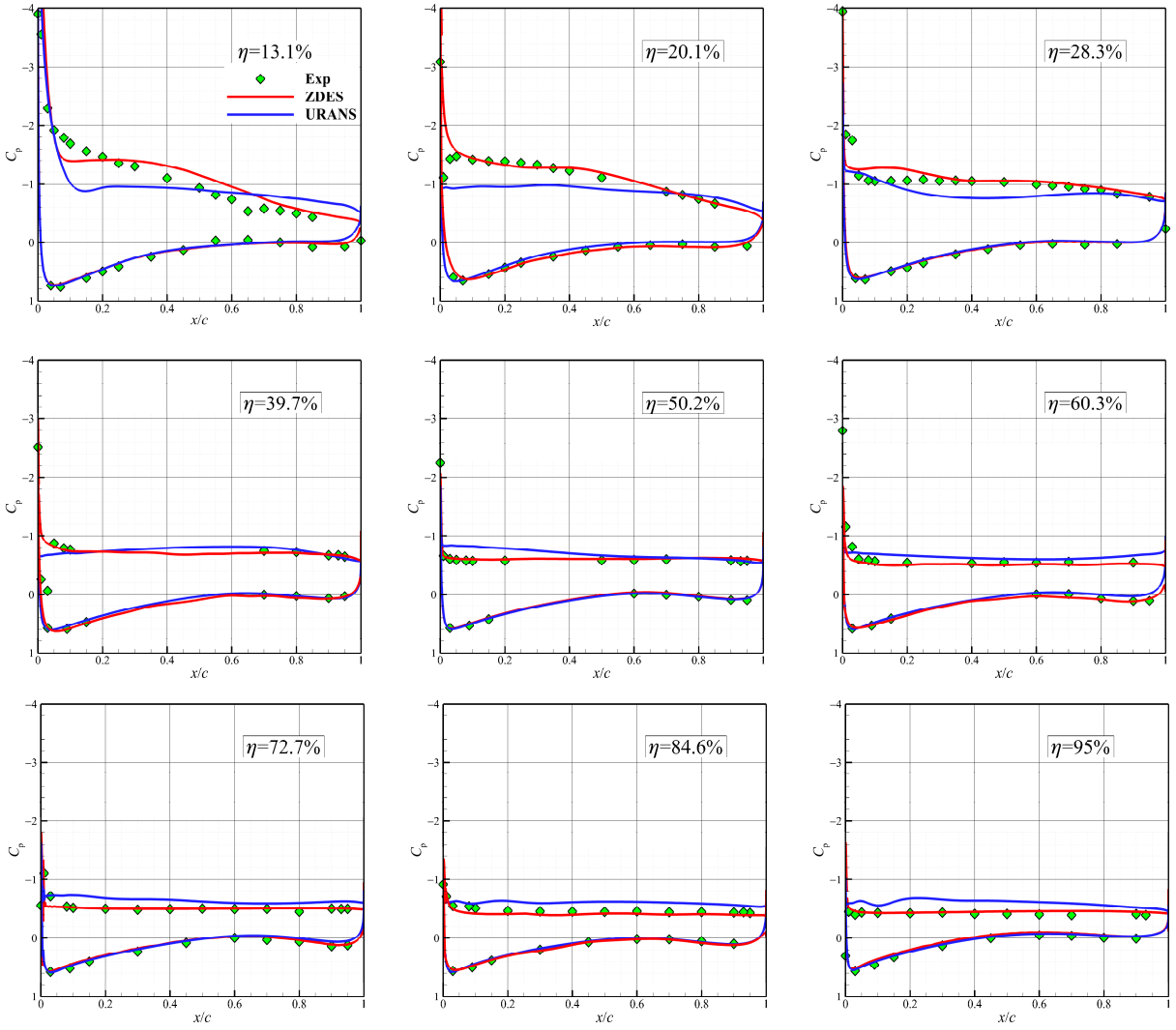

Figure 12. Pressure distribution at each station in the main wing (alpha = 18°).

Figure 13 shows the time-averaged pressure cloud map and the time-averaged streamlines calculated using the URANS and ZDES methods. Comparison of the time-averaged pressure distribution cloud map reveals that there was a significant difference in the low-pressure regions of the inner wing predicted by using the two methods at different angles of attack. The ZDES results showed a larger range of the low-pressure region on the inner wing, extending all the way to the mid-wing section, whereas the low-pressure region predicted using URANS was significantly smaller. The low-pressure region of the inner wing predicted using ZDES increased gradually with the increase in the angle, while the low-pressure region obtained using URANS got smaller and smaller. In particular, the pressure obtained using URANS in the inner wing at 18° was significantly higher than that of the ZDES results, which is the reason why it was a direct reflection of the difference between the two methods in terms of the spanwise position of the inner wing and the experiments, as shown in Figure 12. Meanwhile, the pressure distributions in the outboard region of the horizontal tail were also slightly different between the two methods, which is mainly due to the difference in the prediction of the main wing separation wake between the two methods.

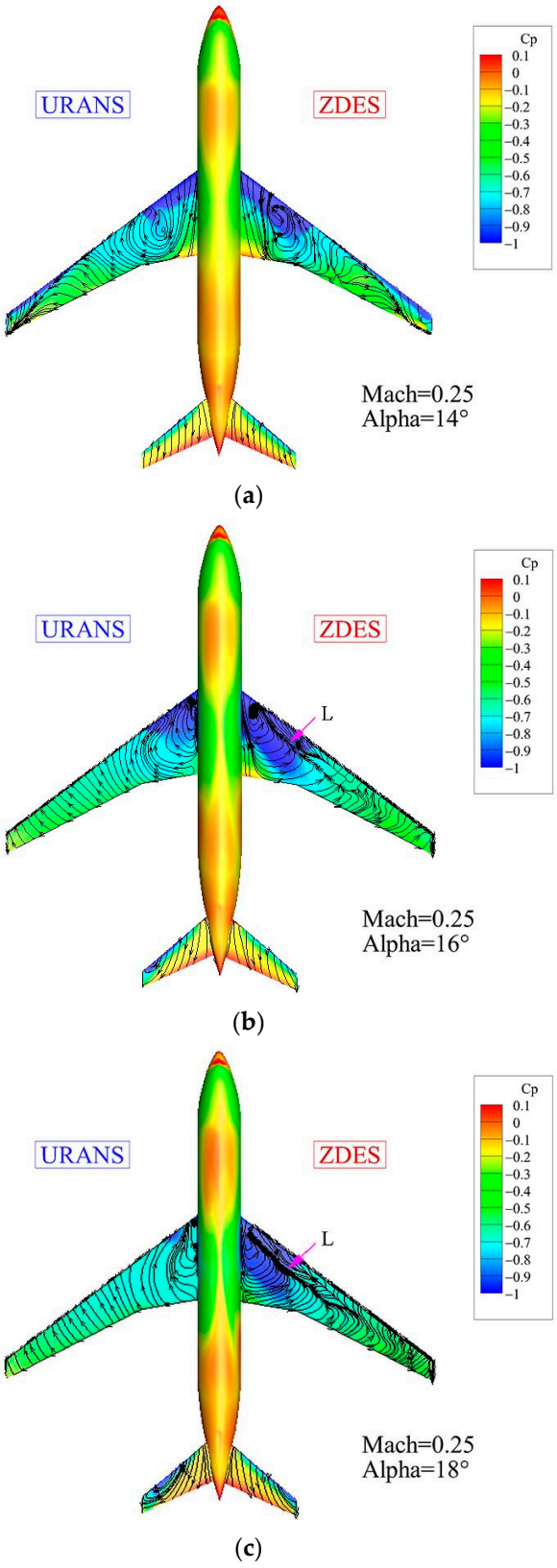

Figure 13. Time-averaged pressure coefficients and streamlines at (**a**) 14°, (**b**) 16°, and (**c**) 18°.

Comparing the time-averaged streamlines obtained using the two methods, at alpha = 16° and 18°, the ZDES results showed a clear flow demarcation line on the main wing, while the URANS results gave smooth streamlines. Due to the stall conditions, the ZDES results

demonstrated more disorganized streamlines, with multiple flow singularities appearing on the upper surface of the main wing, especially in the center and outer wing regions. The URANS results showed a more regular flow, which is a reflection of the difference in the ability of the two methods to analyze the flow structure at different scales.

The difference in pressure distribution was further reflected in the spanwise cross-section. Figure 14 shows the time-averaged streamlines and pressure distributions along the 50% chordwise profile of the main wing for alpha = 18°. From the time-averaged streamlines, it can be found that both the URANS and ZDES flow fields showed two major separation vortices and one minor one, which were the small separation vortices caused by the fuselage profile rectification at the wing–body combination at the lower wing surface, the large separation region in the upper fuselage region, and the large separation vortex in the inner wing region of the main wing, respectively. For the large and small separation vortices above and below the fuselage, there was not much difference between the two prediction methods, and the scales of the separation vortices were basically the same. While the results given by the two methods in the separation region of the inner wing of the main wing were very different, the pressure predicted using URANS was obviously higher, and the separation region was a little smaller than the ZDES results.

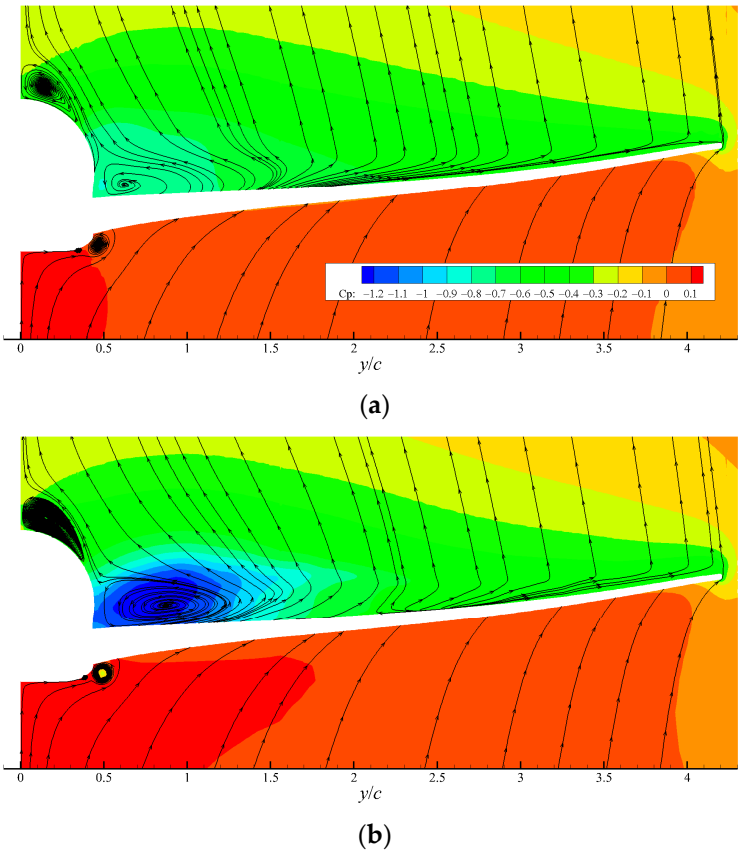

Figure 14. Time-averaged streamlines on the main wing spanwise cross-section: (**a**) URANS and (**b**) ZDES.

Figure 15 shows the spatial time-averaged streamlines obtained from URANS and ZDES calculations for alpha = 18°. The differences between the two methods were large. The ZDES results showed that there was a clear flow demarcation line on the upper wing surface, which was mainly caused by the lateral flow. Under the induced effect of the low-pressure region in the inner wing, a part of the flow in the outer wing flowed laterally along the upper wing toward the inner region. This lateral flow effect also caused time-averaged flow lines L at 16° (Figure 13b) and 18° (Figure 13c). For the mean streamlines of URANS, due to the relatively weak induction of the low-pressure region on the inner wing

and towards the outer wing, the lateral flow effect was also not obvious, and its spatial streamlines showed only the main separating vortex.

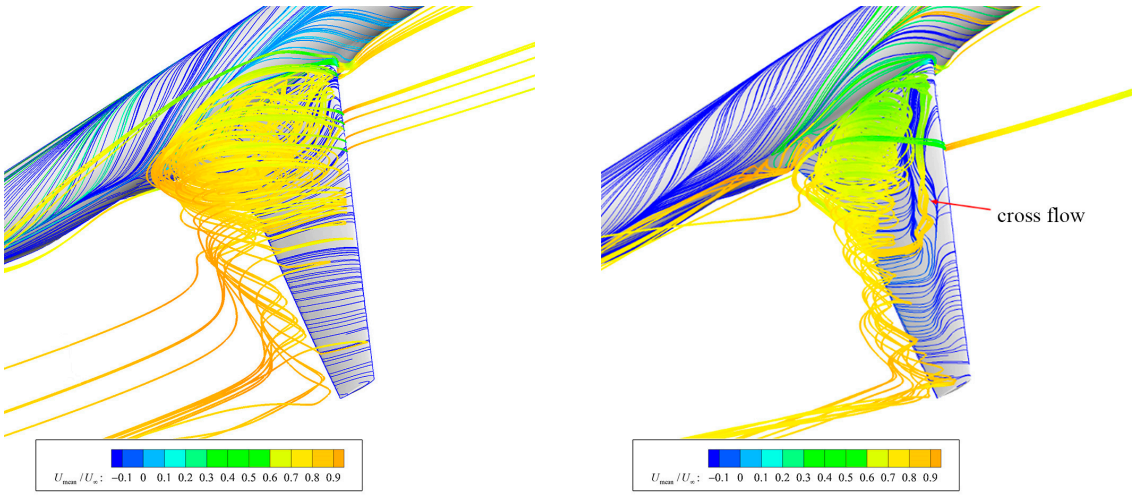

Figure 15. Spatial time-averaged streamlines colored by the dimensionless streamwise velocity (alpha= 18°): (**a**) URANS and (**b**) ZDES.

Figure 16 shows the position of the PIV observation window in the experiment. The center coordinates of the window were x = 328.5 mm, y = 383.1 mm, z = −83.5 mm (the origin was the position of the nose), and the size of the observation window was 54 mm × 112 mm, while the observation plane was located at the η = 59.4% spanwise position at an angle of 21.63° with the Z-axis.

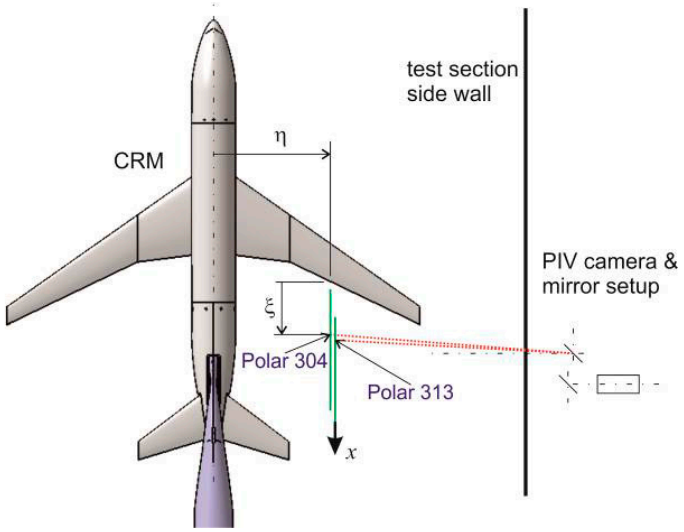

Figure 16. Location of the PIV observation window in the experiment. Reprinted with permission from Ref. [27]. Copyright 2015, Robert Konrath.

Figure 17 shows the comparison of the computed cloud maps of the time-averaged velocity distributions in the flow direction with PIV observations [27] (based on the local coordinates of the PIV observation window). The ZDES results showed that the widths of the main-wing separation regions were in good agreement with the experiment, with a slight discrepancy at the edges of the separation regions, which was mainly due to the fact that the resolution of the computational grid was not sufficient and the grid dissipation

was slightly larger. Compared to the experimental results, the width of the main wing separation area obtained using URANS was significantly too large and the wake area drags were longer compared to the ZDES results, which were in better agreement with the experiment. Figure 18 further gives the calculation results of the time-averaged streamwise velocity profiles at different locations (based on the local coordinates of the PIV observation window), and the width of the wake predicted using the ZDES method in this paper was basically consistent with the PIV results.

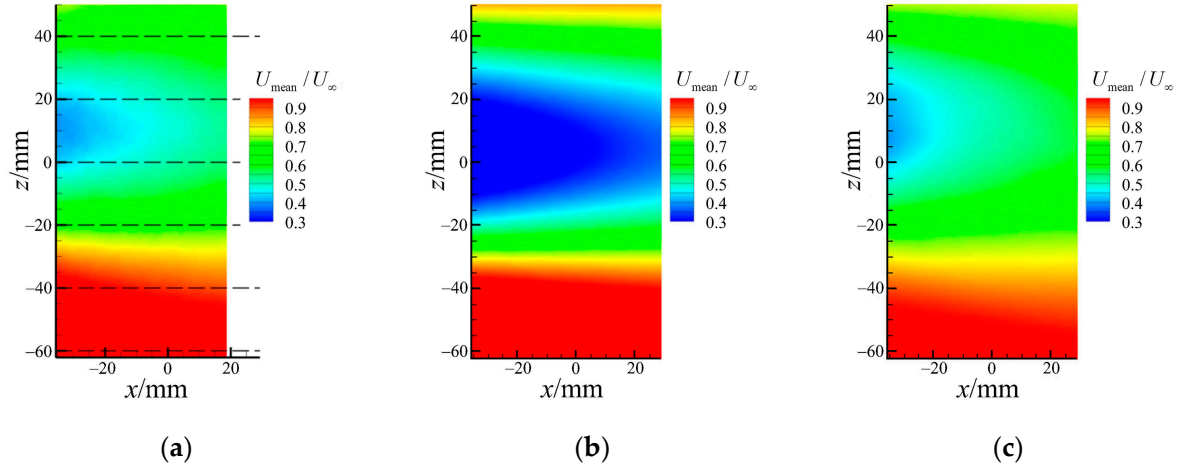

Figure 17. Average flow velocity cloud maps in the wake: (**a**) PIV [27], (**b**) URANS, and (**c**) ZDES.

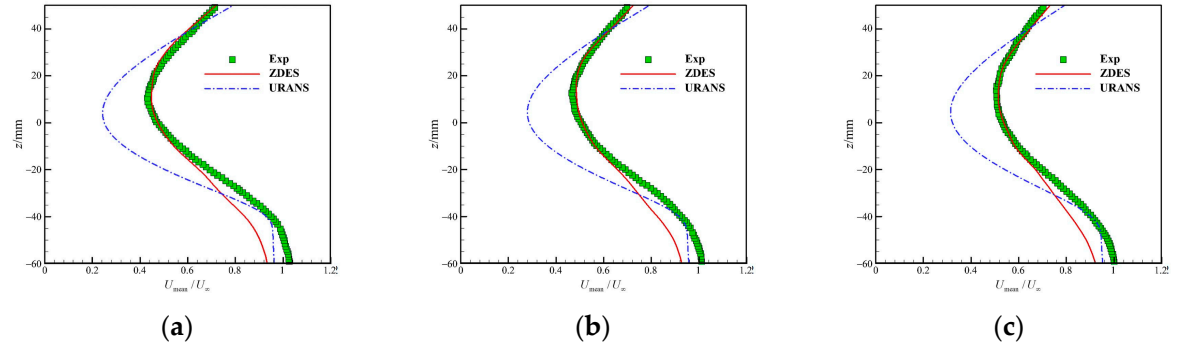

Figure 18. Time-averaged flow velocity profiles in the main wing wake: x = (**a**) −20 mm, (**b**) −5 mm, and (**c**) 10 mm.

The more macroscopic effects of the main wing trailing-edge area can be seen in the mean flow. Figure 19 shows the cloud maps of the computed cross-sectional time-averaged streamlines and time-averaged streamwise velocity distributions for η = 28.3% stations at 18°. The main wing separation region predicted using URANS was significantly larger than the ZDES results. Meanwhile, the downwash effect deflected the streamlines downward in the wake region, and the downwash effects of the two methods were obviously different. The downwash effects were so weak that the streamlines deflected upwards in the main wing wake obtained using URANS, compared with the stronger downwash effect in the ZDES results. The strength of the downwash effect changed the direction of the flow in the main wing wake region, which had an impact on the flow in the horizontal tail region.

Figure 20 shows the instantaneous density gradients obtained from URANS and ZDES calculations for α = 18° (η = 28.3%), and the influence of the downwash effect can also be seen here. In the main wing wake, the ZDES results showed more small-scale turbulent structures, and these small-scale vortices had some interference effects on the horizontal tail during convection downstream. As for the URANS results, the shear layers that shed in the leading and trailing edges of the main wing dissipated quickly and did not form

an effective coupling, which was also consistent with the mean velocity and streamlines, further leading to a weakening of the downwash effect, as well as its relatively weak effect on the wake due to excessive dissipation. The phenomena above led to the pitching moment coefficients obtained from ZDES being consistent with the experiments, while the results from URANS were greater than the ZDES and experiments after stall, as shown in Figure 21.

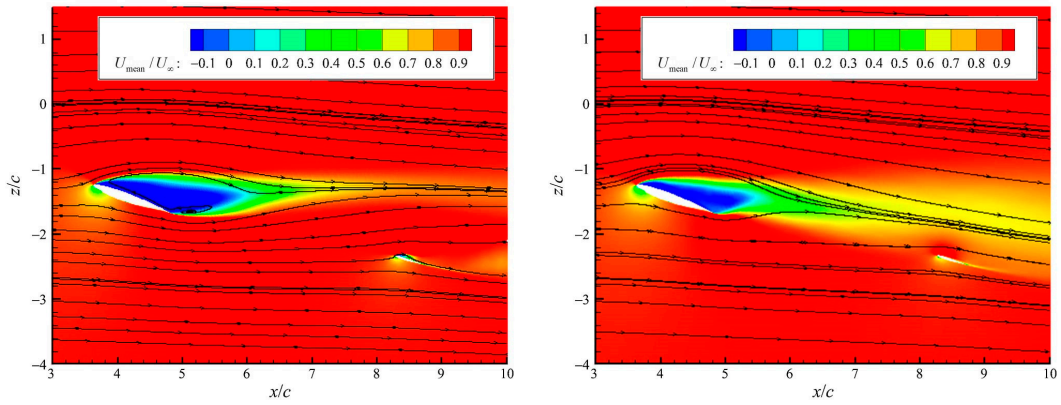

Figure 19. Time-averaged streamlines and streamwise velocity cloud maps in the flow-field cross-sections (alpha = 18°): (**a**) URANS, (**b**) ZDES.

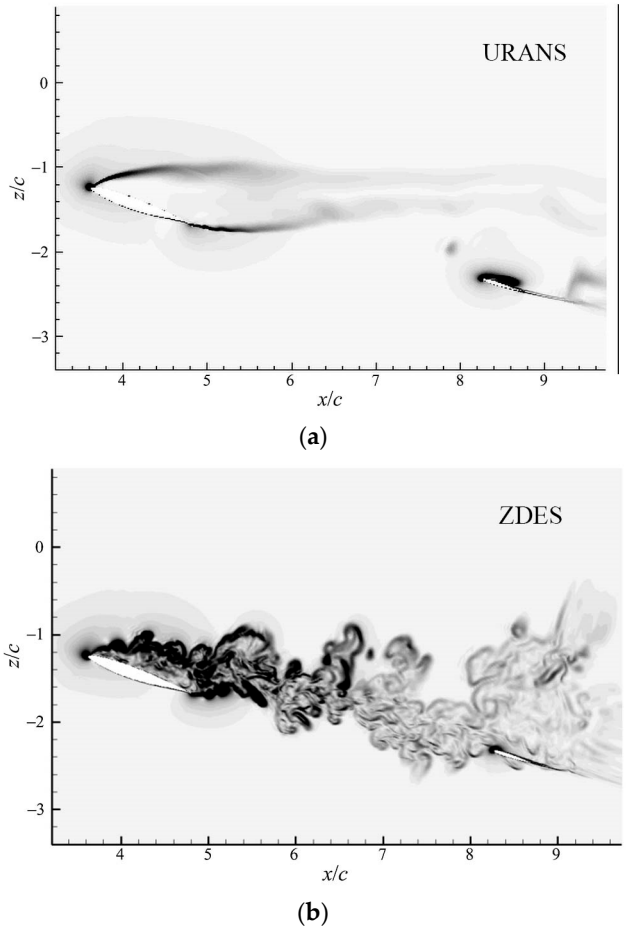

Figure 20. Cloud map of instantaneous density gradient (alpha = 18°): (**a**) URANS, (**b**) ZDES.

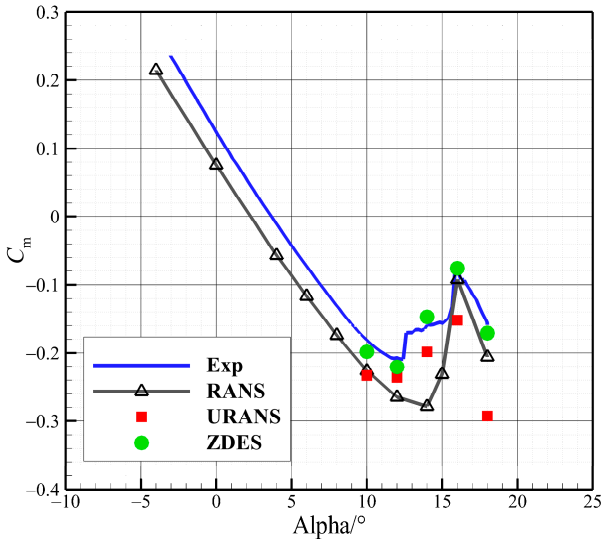

Figure 21. Pitching moment coefficients of the whole aircraft.

Figure 22 shows the instantaneous Q isosurface plots obtained from the ZDES calculations at different angles of attack. The separation region on the main wing gradually expanded from the middle of the wing to the inner wing as the angle increased. The larger-scale vortex structures were formed at the beginning of the main wing shear-layer detachment and gradually broke into more small-scale structures downstream. The different scale vortex structures downstream of the main wing had obvious interference effects on the flow in the horizontal tail region.

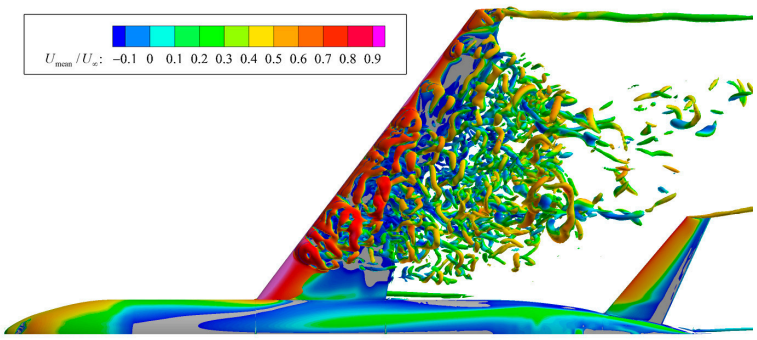

(**a**)

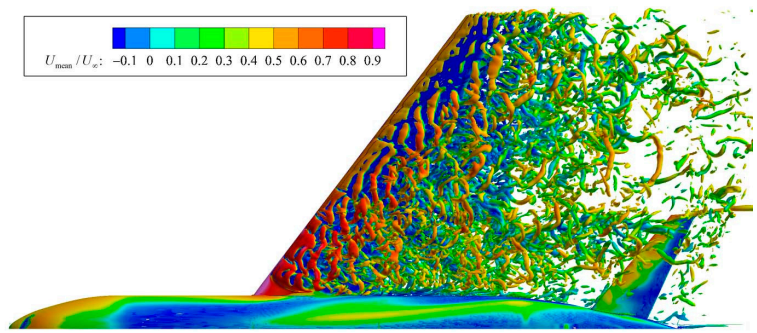

(**b**)

Figure 22. *Cont.*

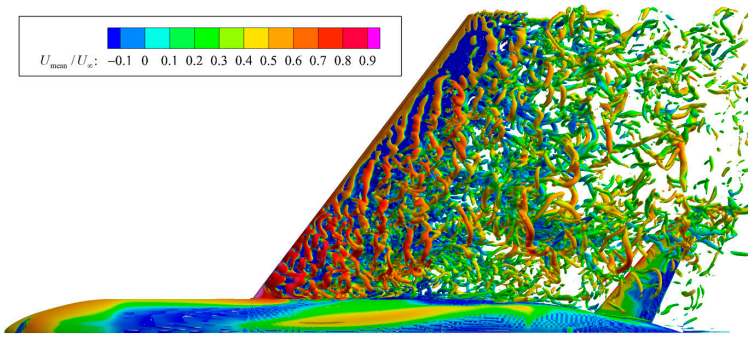

(**c**)

Figure 22. Instantaneous turbulence structures based on a Q-criterion colored by the dimensionless streamwise velocity at (**a**) 14°, (**b**) 16°, and (**c**) 18°.

Figure 23 shows the lift coefficient variations for the whole aircraft, the main wing, and the horizontal tail, respectively, at 18°. Comparing the results of the two methods, the lift coefficients predicted using ZDES changed more drastically and showed large fluctuations with time. In contrast, the lift coefficients obtained using URANS were more stable with time. The variation was relatively flat, with small fluctuations, and this feature was particularly evident in the main wing. This difference between the two methods was mainly due to their different abilities to resolve the small-scale structures in the separation region.

Further analyzing the calculated lift coefficients, it can be seen that the main wing contributed the most to the overall lift, and the difference between the lift coefficients calculated using URANS and ZDES was the largest on the main wing, which was mainly due to the difference in the predictions of the downwash effect on the main wing of the two methods. Under the further influence of the downwash effect, the local angles of attack of the two methods on the horizontal tail were also different, and the strong downwash effect made the local angles of attack of the horizontal tail smaller, which resulted in the lift coefficients of the horizontal tail predicted using ZDES being smaller than those predicted using URANS, which were less affected by the downwash effect.

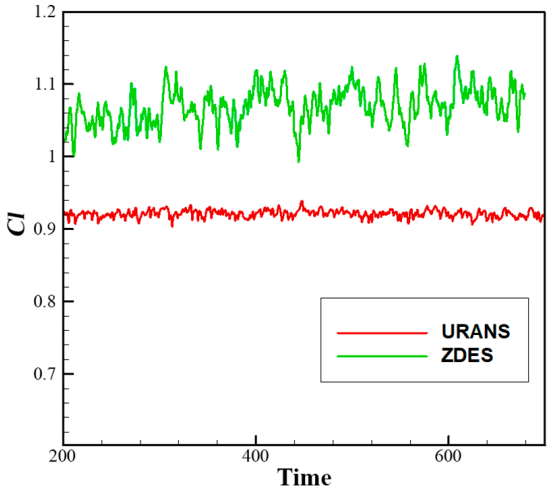

(**a**)

Figure 23. *Cont.*

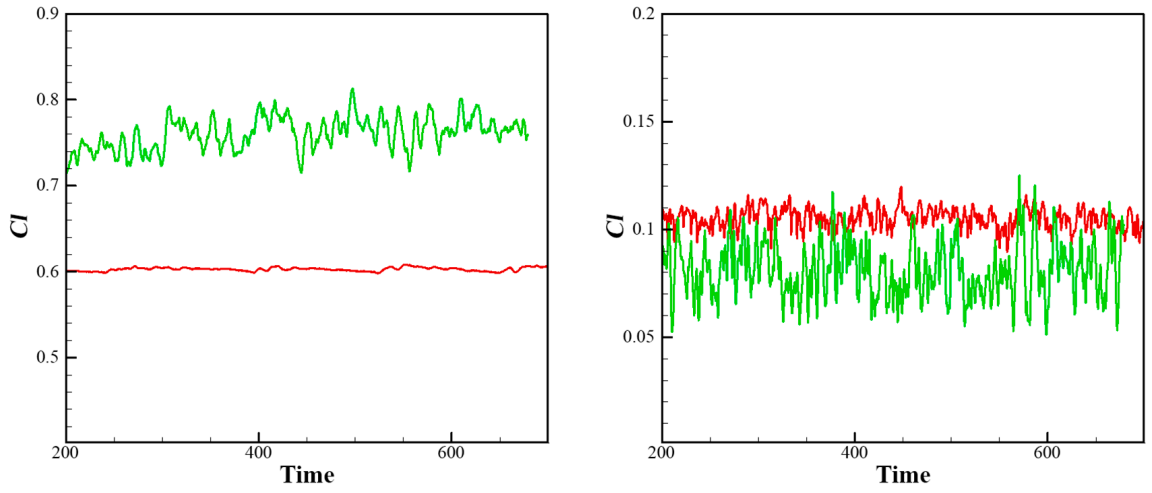

(**b**) (**c**)

Figure 23. Lift coefficient variations in (**a**) the whole aircraft, (**b**) the main wing, and (**c**) the horizontal tail.

Figure 24 shows the lift coefficient fluctuation spectra at different angles of attack. The peaks of the main frequency on the main wing at different angles were basically the same as those of the whole aircraft, which indicates that the influence of the main wing lift change on the whole aircraft played a dominant role. From the lift coefficient spectra of the main wing and the whole aircraft, it can be found that at 14° and 16°, the peaks of the main frequency at the two angles were basically the same and equal to 25 Hz, and the peak of the main frequency at 18° was 13 Hz, which means that the peak of the main frequency began to move towards the low-frequency region with the increase in the angle. The main frequencies at 16° and 18° on the horizontal tail were basically consistent with those on the main wing and the whole aircraft, whereas there were consecutive multiple peaks at 18 Hz, 32 Hz, and 50 Hz at 14°, which were not consistent with those on the main wing and suggest that the main wing wake had less effect on the horizontal tail at 14°.

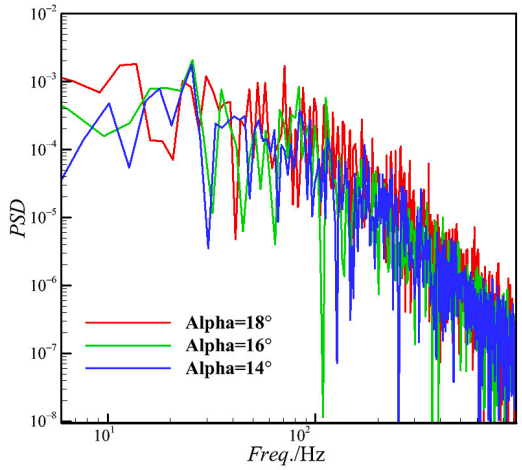

(**a**)

Figure 24. *Cont.*

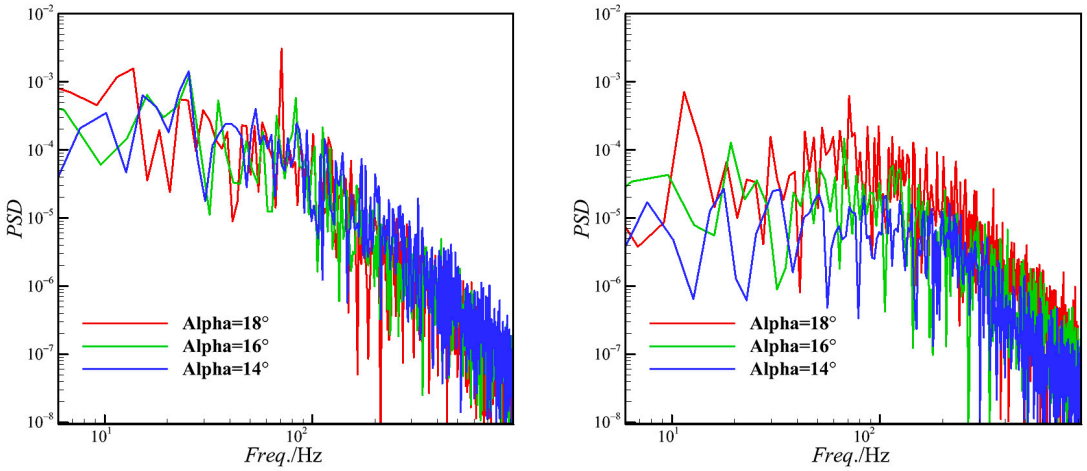

Figure 24. Lift coefficient power spectral densities of (**a**) the whole aircraft, (**b**) the main wing, and (**c**) the horizontal tail.

4. Conclusions

The ZDES method, based on the *k*-*ω* SST turbulence model combined with the low-dissipation Roe format grounded in the fifth-order WENO interpolation, was used to calculate the low-speed aerodynamic characteristics of the CRM wing–body–horizontal-tail configuration. The post-stall aerodynamic characteristics were analyzed by comparing the calculation results of the URANS and ZDES methods. The findings indicated that the ZDES method effectively captured the stall characteristics of the main wing separation region, illustrated the basic morphology of the main wing shear-layer shedding after stall, delineated the influence of the main wing wake on the horizontal tail, and provided a more precise prediction of the entire aircraft's stall characteristics. The specific conclusions of this study can be summarized as follows:

(1) At the post-stall angles of attack, the ZDES results showed a good agreement with the experimental lift coefficients and pressure distributions. The pressure distributions obtained using URANS in the inner wing region deviated more from the experiments, with the predicted separation position advancing and the pressure distributions in the middle and outer wings deteriorating with the increase in the angle. The ZDES results showed a pronounced lateral flow on the wing due to the induction of the low-pressure region of the inner wing; URANS underestimated the low-pressure region of the inner wing after stall, and the predicted low-pressure region of the inner wing diminished as the angle increased. Notably, URANS failed to predict the wing's lateral flow, likely due to a diminished effect induced from the inner wing's low-pressure region.

(2) The ZDES results indicated that the horizontal tail was influenced by the vortices in the wake region of the main wing, primarily due to the downwash effect. With the angle of attack increasing, the separation area on the main wing expanded from the middle of the wing to the inner wing, and the vortex structures in the main wing wake became more complicated. The separation area of the main wing predicted using URANS was too large, and the downwash effect was weakened due to the dissipation of the shear layer that was too fast and the lack of effective coupling, which made the predicted lift and drag coefficients differ from the experiments. The lift coefficient of the horizontal tail obtained using ZDES was smaller than that obtained using URANS due to the downwash effect altering local angles of attack.

(3) The lift coefficients predicted using ZDES fluctuated more drastically over time, and the main peak of the lift coefficient spectrum moved to the low-frequency region as the angle of attack increased, and the influence of the main wing's wake on the horizontal tail

was smaller at alpha = 14°. Due to the inadequate resolution of the small-scale structures, the lift coefficients obtained using URANS showed limited non-stationary characteristics.

Author Contributions: Conceptualization, H.Z. and J.L.; methodology, H.Z.; software, J.L.; validation, X.Z., H.Z. and J.L.; formal analysis, X.Z.; investigation, X.Z.; resources, X.Z.; data curation, X.Z.; writing—original draft preparation, X.Z.; writing—review and editing, X.Z., H.Z. and J.L.; visualization, X.Z.; supervision, H.Z.; project administration, J.L.; funding acquisition, J.L. All authors have read and agreed to the published version of the manuscript.

Funding: This research was funded by National Natural Science Foundation of China, grant number 11972304.

Data Availability Statement: Not applicable.

Conflicts of Interest: The authors declare no conflict of interest.

References

1. Forsythe, J.R.; Squires, K.D.; Wurtzler, K.E.; Spalart, P.R. Detached-eddy simulation of the F-15E at high alpha. *J. Aircr.* **2004**, *41*, 193–200. [CrossRef]
2. Forsythe, J.R.; Woodson, S.H. Unsteady computations of abrupt wing stall using detached-eddy simulation. *J. Aircr.* **2005**, *42*, 606–616. [CrossRef]
3. Morton, S.; Steenman, M.; Cummings, R.; Forsythe, J. DES grid resolution issues for vortical flows on a delta wing and an F-18C. In Proceedings of the 41st Aerospace Sciences Meeting and Exhibit, Reno, Nevada, 6–9 January 2003.
4. Tomac, M.; Jirasek, A.; Rizzi, A. Hybrid Reynolds-Averaged Navier–Stokes/Large-Eddy Simulations of F-16XL in Low-Speed High-Alpha Flight. *J. Aircr.* **2017**, *54*, 2070–2076. [CrossRef]
5. Fu, S.; Xiao, Z.; Chen, H.; Zhang, Y.; Huang, J. Simulation of wing-body junction flows with hybrid RANS/LES methods. *Int. J. Heat Fluid Flow* **2007**, *28*, 1379–1390. [CrossRef]
6. Xiao, Z.; Chen, H.; Zhang, Y.; Huang, J.; Fu, S. Study of delayed-detached eddy simulation with weakly nonlinear turbulence model. *J. Aircr.* **2006**, *43*, 1377–1385. [CrossRef]
7. Waldmann, A.; Gansel, P.P.; Lutz, T.; Krämer, E. Unsteady wake of the NASA common research model in low-speed stall. *J. Aircr.* **2015**, *53*, 1073–1086. [CrossRef]
8. Lutz, T.; Gansel, P.P.; Waldmann, A.; Zimmermann, D.-M.; Hülse, S.S.A. Prediction and Measurement of the Common Research Model Wake at Stall Conditions. *J. Aircr.* **2016**, *53*, 501–514. [CrossRef]
9. Spalart, P.R. Comments on the feasibility of LES for wings, and on a hybrid RANS/LES approach. In Proceedings of the First AFOSR International Conference on DNS/LES, Ruston, LA, USA, 4–8 August 1997; Liu, C., Liu, Z., Eds.; Greyden: Columbus, OH, USA, 1997; pp. 137–147.
10. Spalart, P.R.; Deck, S.; Shur, M.L.; Squires, K.D.; Strelets, M.K.; Travin, A. A new version of detached-eddy simulation, resistant to ambiguous grid densities. *Theor. Comput. Fluid Dyn.* **2006**, *20*, 181–195. [CrossRef]
11. Menter, F.R.; Kuntz, M. Adaptation of eddy-viscosity turbulence models to unsteady separated flow behind vehicles. In *the Aerodynamics of Heavy Vehicles: Trucks, Buses and Trains*; Mccallen, R., Browand, F., Ross, J., Eds.; Springer: Berlin/Heidelberg, Germany, 2004; pp. 339–352.
12. Fröhlich, J.; von Terzi, D. Hybrid LES/RANS methods for the simulation of turbulent flows. *Prog. Aerosp. Sci.* **2008**, *44*, 349–377. [CrossRef]
13. Mockett, C. A Comprehensive Study of Detached-Eddy Simulation. Technical University Berlin: Berlin, Germany, 2009.
14. Deck, S. Recent improvements in the Zonal Detached Eddy Simulation (ZDES) formulation. *Theor. Comput. Fluid Dyn.* **2012**, *26*, 523–550. [CrossRef]
15. Menter, F.R. Two-equation eddy-viscosity turbulence models for engineering applications. *AIAA J.* **1994**, *32*, 1598–1605. [CrossRef]
16. Launder, B.E.; Spalding, D.B. The numerical computation of turbulent flows. *Comput. Methods Appl. Mech. Eng.* **1974**, *3*, 269–289. [CrossRef]
17. Wilcox, D.C. Reassessment of the scale-determining equation for advanced turbulence models. *AIAA J.* **1988**, *26*, 1299–1310. [CrossRef]
18. Wilcox, D.C. Comparison of two-equation turbulence models for boundary layers with pressure gradient. *AIAA J.* **1993**, *31*, 1414–1421. [CrossRef]
19. Wilcox, D.C. *Turbulence Modeling for CFD*; DCW Industries: La Canada, CA, USA, 1998.
20. Wilcox, D.A. Simulation of transition with a two-equation turbulence model. *AIAA J.* **1994**, *32*, 247–255. [CrossRef]
21. Menter, F.R. Performance of popular turbulence model for attached and separated adverse pressure gradient flows. *AIAA J.* **1992**, *30*, 2066–2072. [CrossRef]
22. Chauvet, N.; Deck, S.; Jacquin, L. Zonal Detached Eddy Simulation of a Controlled Propulsive Jet. *AIAA J.* **2007**, *45*, 2458–2473. [CrossRef]

23. Vassberg, J.; Dehaan, M.; Rivers, M.; Wahls, R. Development of a common research model for applied CFD validation studies. In Proceedings of the 26th AIAA Applied Aerodynamics Conference, Honolulu, HI, USA, 18–21 August 2008; p. 6919.
24. Vassberg, J.C.; Tinoco, E.N.; Mani, M.; Rider, B.; Zickuhr, T.; Levy, D.W.; Brodersen, O.P.; Eisfeld, B.; Crippa, S.; Wahls, R.A.; et al. Summary of the fourth AIAA computational fluid dynamics drag prediction workshop. *J. Aircr.* **2014**, *51*, 1070–1089. [CrossRef]
25. Hefer, G. ETW-A facility for high Reynolds number testing. In Proceedings of the IUTAM Symposium Transsonicum IV: Proceedings of the IUTAM Symposium, Göttingen, Germany, 2–6 September 2002; Springer: Berlin/Heidelberg, Germany, 2003; pp. 157–164.
26. Yang, Z.; Li, J.; Jin, J.; Zhang, H.; Jiang, Y. Investigation and improvement of stall characteristic of High-Lift configuration without slats. *Int. J. Aerosp. Eng.* **2019**, *2019*, 7859482. [CrossRef]
27. Konrath, R. High-speed PIV applied to wake of NASA CRM model in ETW under high re-number stall conditions for sub-and transonic speeds. In Proceedings of the 53rd AIAA Aerospace Sciences Meeting, Kissimmee, FL, USA, 5–9 January 2015; p. 1095.